A new mouse model of radiation-induced liver disease reveals mitochondrial dysfunction as an underlying fibrotic stimulus
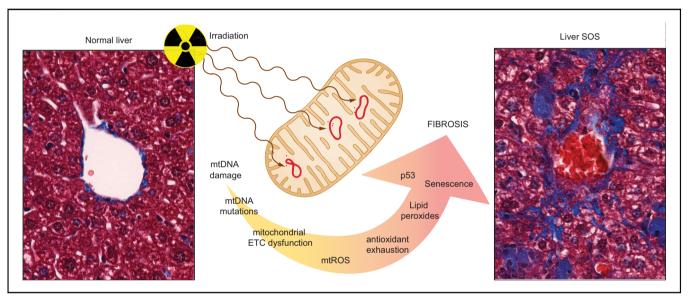
Authors

Nicolas Melin, Tural Yarahmadov, Daniel Sanchez-Taltavull, Fabienne E. Birrer, Tess M. Brodie, Benoît Petit, Andrea Felser, Jean-Marc Nuoffer, Matteo Montani, Marie-Catherine Vozenin, Evelyn Herrmann, Daniel Candinas, Daniel M. Aebersold, Deborah Stroka

Correspondence

deborah.stroka@dbmr.unibe.ch (D. Stroka).

Graphical abstract

Highlights

- New mouse model of radiation-induced liver fibrosis using image-guided radiation.

- Irradiated tissue develops pericentral fibrosis 6 weeks post-irradiation.

- Irradiation induces hepatic mitochondrial DNA mutagenesis.

- Hepatocyte irradiation provokes mitochondrial dysfunction.

- Irradiation increases ROS, p53 and senescence signaling leading to hepatic fibrosis.

Lay summary

Irradiation is an efficient cancer therapy, however, its applicability to the liver is limited by life-threatening radiation-induced hepatic fibrosis. We have developed a new mouse model of radiation-induced liver fibrosis, that recapitulates the human disease. Our model highlights the role of mitochondrial DNA instability in the development of irradiation-induced liver fibrosis. This new model and subsequent findings will help increase our understanding of the hepatic reaction to irradiation and to find strategies that protect the liver, enabling the expanded use of radiotherapy to treat hepatic tumors.

A new mouse model of radiation-induced liver disease reveals mitochondrial dysfunction as an underlying fibrotic stimulus

Nicolas Melin,[1,2] Tural Yarahmadov,[1,2] Daniel Sanchez-Taltavull,[1,2] Fabienne E. Birrer,[1,2] Tess M. Brodie,[1,2] Benoît Petit,[3] Andrea Felser,[4] Jean-Marc Nuoffer,[4] Matteo Montani,[5] Marie-Catherine Vozenin,[3] Evelyn Herrmann,[6] Daniel Candinas,[1] Daniel M. Aebersold,[6] Deborah Stroka[1,2,*]

[1]Department of Visceral Surgery and Medicine, Inselspital, Bern University Hospital, University of Bern, Switzerland; [2]Department for BioMedical Research, Visceral Surgery and Medicine, University of Bern, Switzerland; [3]Laboratory of Radiation Oncology, Radiation Oncology Service, Department of Oncology, CHUV, Lausanne University Hospital, University of Lausanne, Switzerland; [4]Institute of Clinical Chemistry, University of Bern, Switzerland; [5]Department of Pathology, University of Bern, Switzerland; [6]Department of Radiation Oncology, Department for BioMedical Research, University of Bern, Bern University Hospital, Switzerland

Background & Aims: High-dose irradiation is an essential tool to help control the growth of hepatic tumors, but it can cause radiation-induced liver disease (RILD). This life-threatening complication manifests itself months following radiation therapy and is characterized by fibrosis of the pericentral sinusoids. In this study, we aimed to establish a mouse model of RILD to investigate the underlying mechanism of radiation-induced liver fibrosis.
Methods: Using a small animal image-guided radiation therapy platform, an irradiation scheme delivering 50 Gy as a single dose to a focal point in mouse livers was designed. Tissues were analyzed 1 and 6 days, and 6 and 20 weeks post-irradiation. Irradiated livers were assessed by histology, immunohistochemistry, imaging mass cytometry and RNA sequencing. Mitochondrial function was assessed using high-resolution respirometry.
Results: At 6 and 20 weeks post-irradiation, pericentral fibrosis was visible in highly irradiated areas together with immune cell infiltration and extravasation of red blood cells. RNA sequencing analysis showed gene signatures associated with acute DNA damage, p53 activation, senescence and its associated secretory phenotype and fibrosis. Moreover, gene profiles of mitochondrial damage and an increase in mitochondrial DNA heteroplasmy were detected. Respirometry measurements of hepatocytes *in vitro* confirmed irradiation-induced mitochondrial dysfunction. Finally, the highly irradiated fibrotic areas showed markers of reactive oxygen species such as decreased glutathione and increased lipid peroxides and a senescence-like phenotype.
Conclusions: Based on our mouse model of RILD, we propose that irradiation-induced mitochondrial DNA instability contributes to the development of fibrosis via the generation of excessive reactive oxygen species, p53 pathway activation and a senescence-like phenotype.
Lay summary: Irradiation is an efficient cancer therapy, however, its applicability to the liver is limited by life-threatening radiation-induced hepatic fibrosis. We have developed a new mouse model of radiation-induced liver fibrosis, that recapitulates the human disease. Our model highlights the role of mitochondrial DNA instability in the development of irradiation-induced liver fibrosis. This new model and subsequent findings will help increase our understanding of the hepatic reaction to irradiation and to find strategies that protect the liver, enabling the expanded use of radiotherapy to treat hepatic tumors.

Introduction

High-dose irradiation is an effective treatment to control primary liver cancer and the regression of hepatic metastasis.[1,2] Moreover, it can increase immunoreactivity towards tumors when used alone or in combination with new immune-targeted therapies, opening new options for the treatment of liver cancers.[3] Unfortunately, the applicability of radiation therapy in the liver is restricted by the adverse reaction of the normal liver tissue to radiation that can lead to organ dysfunction and failure. Radiation-induced liver disease (RILD) develops slowly over months post-irradiation, with symptoms including jaundice, tender hepatomegaly, ascites, and sudden weight gain.[4] No histological changes are visible in the liver tissue during the latency phase, however, during the symptomatic stage, there is an increase in collagen fibers in the centrilobular sinusoids and extravasation of red blood cells resulting in a life-threatening condition called sinusoidal obstruction syndrome (SOS).[5]

Although many clinical investigations have been performed to estimate the risk of developing RILD based on liver health, radiation dose, and irradiated liver volume,[6] less is known about mechanisms that lead to the development of RILD and, more specifically, SOS.

RILD is a complex multicellular process that evolves over time and understanding the mechanisms underlying disease development has benefitted from robust animal modelling. Models in rats and non-human primates have been established[7,8] as well as 2 strategies in mice, either using low-dose irradiation with long-term follow-up or high-dose irradiation to study immediate effects.[9–11] These models identified the importance of TGF-β, hedgehog signaling, and gender sensitivity. However, these models did not lead to SOS, thus there are still unanswered questions regarding the factors leading to SOS and the underlying mechanism of RILD remains elusive. Herein, we describe a novel mouse model of RILD, using image-guided radiation therapy (IGRT), in which the pathological features of SOS began to emerge 6-weeks post-irradiation. In addition, our analysis of the irradiated liver tissue reveals that radiation-induced mitochondrial dysfunction may be an initiating stimulus responsible for the development of SOS.

Materials and methods

Animal handling, imaging, and irradiation

Eight-week-old BALB/c female mice (Charles River Laboratories, Saint-Germain-Nuelles, France) were used for this experiment based on their described radiosensitivity and ability to develop a hepatic fibrotic response.[12,13] Mice were acclimatized in a temperature-controlled room under a 12 h dark/light cycle with *ad libitum* access to water and standard purified diet (D01060501, Research Diets) for 2 weeks prior to the irradiation and until the experimental endpoint. CT-imaging and irradiation were performed during the light phase under 2% isoflurane anesthesia using an X-Rad 225cx small animal irradiator (Precision X-Ray). Mice were injected with 50 µl iv of ExiTron nano6000 contrast agent (Miltenyi Biotec) in which no liver and kidney toxicity was observed (Fig. S1). The dose of irradiation was calculated by Monte Carlo dose calculation (SmART-Plan X-rad 225cx planning system, Precision X-Ray), and delivery was performed using a Varian Tube NDI 226 (X-ray machine; 250 keV, tube current: 15 mA, beam filter: 5 mm Cu), with a dose rate of 1.08 Gy·min^{-1}. Reversible alopecia was noted on the abdomen of the irradiated animals without skin ulceration. At experimental endpoints, mice were placed under general anesthesia (i.p. injection of fentanyl (Hameln) 50 µg/kg, midazolam (Roche) 5 mg/kg, medetomidine (Virbacc) 500 µg/kg), and heparin 500 U/kg (iv, Bichsel AG) and were sacrificed by exsanguination through the portal vein. Liver tissues were excised, partitioned into low- and high-irradiated samples, and fixed in 4% formalin for paraffin embedding, and 1-3 mm^3 liver pieces were snap frozen in liquid nitrogen and stored at −80°C. Experiments were approved by the local animal authorities and in strict accordance with good animal practice as defined by the Office of Laboratory Animal Welfare.

RNA sequencing

RNA was extracted from snap-frozen tissue with the RNeasy Micro Kit (Qiagen) quantified by the Qubit BR assay (Thermo Fisher Scientific) and quality was assessed by Fragment Analyzer (Advanced Analytical) using the Standard Sensitivity RNA Analysis Kit (Advanced Analytical). Libraries were prepared without size exclusion with the TruSeq Stranded mRNA kit (Illumina). Qubit double-stranded DNA high sensitivity (Thermo Fisher Scientific) and Fragment Analyzer NGS (Advanced Analytical) kits were used for library quality control. Finally, the samples were sequenced on a HiSeq3000 (Illumina), 1x100 bp on 4.5 lanes.

RNA expression analysis

Transcriptomic analysis was performed based on the RNA sequencing (RNAseq) results and bioinformatics methods described in the supplementary information.

mtDNA sequences analysis

Mitochondrial DNA (mtDNA) sequences were retrieved from the RNAseq data (methods are described in the supplementary information).

Histology and immunohistochemistry

Four µm thick paraffin sections were stained with H&E, Masson's trichrome, and Prussian Blue for histological analysis. Immunohistochemistry was performed using the primary antibodies, and biotinylated secondary antibodies listed in Table S1. Antibody complexes were detected with peroxidase-labeled streptavidin (KPL SeraCare) and 3,3'-diaminobenzidine chromogenic reaction (Sigma-Aldrich), then imaged with the Panoramic MIDI Scanner with 20x objective (3DHISTECH).

Imaging mass cytometry

Paraffin sections, 3.5 µm thick, were stained using the 18-antibody imaging mass cytometry (IMC) panel (Table S2) optimized for formalin-fixed mouse tissue [50]. Briefly, tissues were stained with a single cocktail of metal-labeled antibodies and acquired on the IMC platform's Hyperion tissue imager (Fluidigm). The resulting files were analyzed using histoCAT web[14] for quality control and visualization, and target overlay images were exported as PNGs.

In vitro hepatocyte experiments

Hepatocytes were isolated from BALB/c mouse via 2-step collagenase perfusion (method described in the supplementary information). Twenty-four hours after plating, hepatocytes were irradiated with 50 Gy using a Gammacell® 40 (Best Theratronics Ltd.), and analyzed 6 days post-irradiation for glutathione content and for respirometry.

Glutathione measurements

Glutathione levels were measured from mouse hepatocytes in culture and irradiated liver tissue using the Quantification kit for oxidized and reduced glutathione (Sigma).

High-resolution respirometry

Hepatocytes were detached from culture plates using Collagenase H (Roche), permeabilized with digitonin (10 µg/1 million cells), and oxygen consumption was measured using an Oxygraph-2k high-resolution respirometer equipped with DatLab software (Oroboros Instruments) (methods are described in the supplementary information).

Results

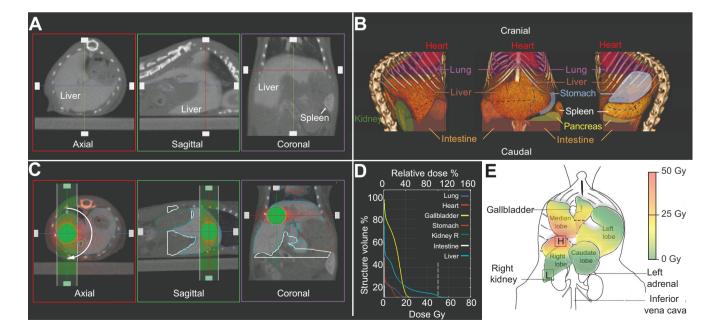### Irradiation plan for mouse RILD model

To establish a mouse model of RILD we used the X-Rad 225cx small animal IGRT platform to deliver a high dose of radiation precisely to the liver. The position of the liver within the abdominal cavity was visualized using ExiTron nano6000 contrasting agent and CT (Fig. 1A). The mouse liver was found to be positioned throughout the upper abdomen in close proximity with surrounding organs (Fig. 1B). We designed a 180° arc irradiation plan using a 5 mm diameter collimator to deliver 50 Gy as a single dose to an isocenter located at the right superior lobe and median lobe interface (Fig. 1C). With this plan, 1% of the liver volume received the full 50 Gy dose and the dose delivered to the surrounding organs was less than 20 Gy with not more than 20% of the stomach and lung exposed (Fig. 1D). Within the liver, we expected a dose shading emanating from the isocenter extending across the right superior and the cranial end of the median and left lobes. Finally, the irradiation plan spared the right inferior and caudal part of the median and left lobes with approximately 50% of the liver not exposed to direct irradiation (Fig. 1E).

Histological assessment of irradiated livers

To capture multiple steps during the development of RILD, we analyzed livers at day-1 for early responses to radiation, at day-6 for the latency phase, at week-6 for signs of fibrosis, and at week-20 for long-term effects (Fig. 2A). In a model of chemotherapy-induced SOS, signs of perisinusoidal dilatation and collagen deposition appeared after 5 weeks of treatment.[15] In our study, mice did not show signs of distress or acute toxicity during the 20-week follow-up, nor did transaminase or bilirubin levels increase at the 4 tested time points (Fig. S2). We evaluated the histopathology of the left and right-median liver lobes, which
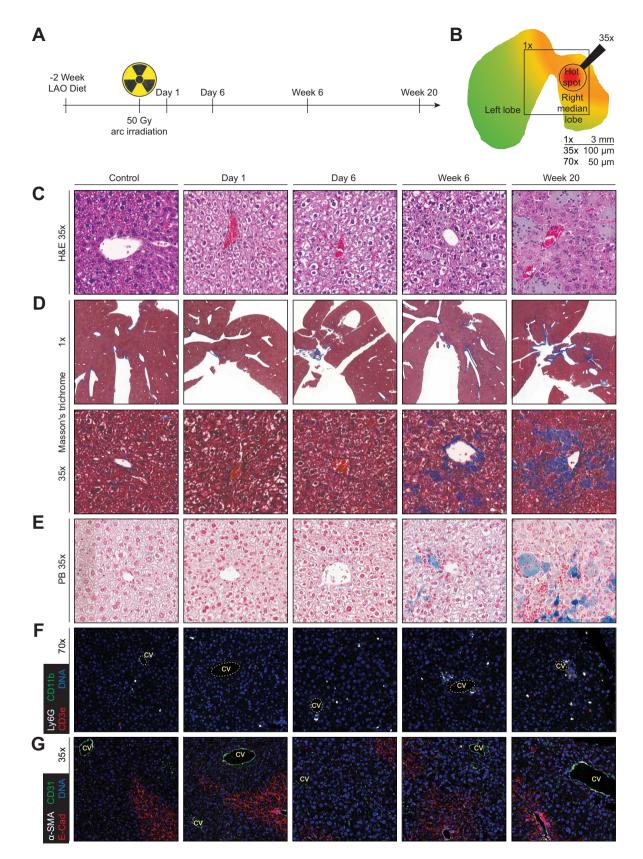
covered the isocenter of the high-irradiated right superior lobe (annotated as HIGH) with shading down to the very LOW-irradiated areas (annotated as LOW) (Fig. 2B). No histological changes were observed by H&E staining at day-1 and day-6 post-irradiation compared to control livers. However, at week-6 and even more prominent at week-20, giant non-eosin-stained cells accumulated around the central vein in the HIGH-irradiated area, and an increase of collagen was visible (Fig. 2C). Collagen deposition was confirmed using a Masson's trichrome stain and an aniline blue signal was observed in the hotspot area at week-6 and at week-20 at low magnification (1x). At higher magnification (35x), collagen fibers were detected between hepatocytes in the central vein region at 6 and 20 weeks, and increased in intensity and distance from the central regions with time (Fig. 2D). Also, at week-20, collagen fiber deposition extended further beyond the hotspot area into the cranial part of the left lobe (Fig. S3). The irradiated liver tissue was stained with Prussian blue to demonstrate that the giant cells observed at 6 and 20 weeks are iron-containing cells (Fig. 2E). This observation led us to question if they are immune cells; thus, we further explored the immune cell composition using IMC and a 17-target antibody panel (Table S2 and Fig. S4). Immune cells were identified by their linage markers, and compared to control and day-1 livers, we observed a slight increase of neutrophils (Ly6G), macrophages (CD11b), and T cells (CD3e) 6 days after irradiation (Fig. 2F). At later time points, those immune cells were found to cluster near the central veins (Fig. 2F). Additionally, we evaluated the stellate cell activation using α-SMA and overlayed it with the hepatic zonation marker E-cadherin, and the endothelial marker CD31, and the nucleus (DNA). In control livers, cells expressing α-SMA were found mostly in portal regions with a few cells identified around the central veins. Irradiation did not increase α-SMA in the portal region, in the pericentral sinusoid or in the

Fig. 1. Image-guided irradiation plan. Mouse liver is imaged by CT using a liver/spleen targeting contrast agent (A), allowing a 3D reconstruction of the liver in the abdominal cavity (B). The irradiation plane of a 50 Gy single-dose irradiation using a 180° arc irradiation (C). The dose-volume histogram depicting the dose delivered on the x-axis and the volume of the organ irradiated on the y-axis (D). A schematic view of the delivered doses allows to visually locate the dose delivered to the different liver lobe and the liver pieces used for the paired transcriptomic analysis; H for HIGH-irradiated, and L for LOW-irradiated (E).

Fig. 2. 50 Gy local liver irradiation leads to SOS and immune cell infiltration. Mice were fed with a LAO diet starting 2 weeks before the irradiation and during the experiment. The livers were collected at day-1 (n = 4), day-6 (n = 4), week-6 (n = 4), and week-20 (n = 3) (A). Schematic representation of the doses delivered to the left and median lobe. Histological evaluation focusing on the annotated hot spot (B). Histological evaluation of the livers using H&E staining (C), Masson's trichrome staining (D), and Prussian blue (E). Imaging mass cytometry visualization of Ly6G, CD3e, CD11b, and DNA (F), and E-cadherin, CD31, α-SMA, and DNA (G) around the CV. CV, central vein; LAO, low antioxidant; SOS, sinusoidal obstruction syndrome.

region of the central vein (Fig. 2G). This absence of increased α-SMA post-irradiation suggests that pericentral fibrosis is not dependent on HSC activation but rather on reactions in the pericentral cells. Taken together, after the initial latent phase, the liver developed typical characteristics of SOS such as collagen deposition in the pericentral sinusoids in the HIGH-irradiated areas, and the formation of immune cell clusters near the central veins.

Radiation-induced fibrosis is a dynamic process

We next investigated the time-dependent transcriptional changes following irradiation to gain further insight into the mechanisms driving RILD. Using RNAseq, we studied the transcriptome of livers of each mouse from the HIGH- and LOW-irradiated areas (Fig. 1E). The principal component analysis showed a time-dependent clustering of the samples (Fig. S5). With each time point analyzed separately, the subsequent 4 principal component analyses showed a clear separation between the HIGH and LOW samples. The effect of irradiation was consistent between mice at each time point and the non-irradiated control samples clustered with proximity to the LOW samples (Fig. 3A). Next, a list of the differentially expressed genes was generated using a paired analysis for each time point. More than 5,500 genes at day-1, 91 genes on day-6, >700 genes at week-6, and >2,500 genes at week-20 were differentially regulated (Fig. 3B). There was limited overlap of regulated genes between time points, suggesting that radiation-induced fibrosis is a process that is evolving (Fig. 3C,D). Pathway enrichment analysis resulting from the comparison of HIGH and LOW samples at day 1 showed acute responses to radiation, such as DNA damage response (Fig. S6), cell cycle regulation, and oxidative stress responses, as well as pathways associated with chromatin organization, RNA transcription, protein synthesis and modification, mitochondrial organization and sterol, amino acid, and carbon metabolism (Fig. 3E and Fig. S7). Interestingly, on day-6 post-irradiation, there were only 91 genes that were differentially regulated, using a *p* value cut-off of <0.05; therefore, we included all the differentially expressed genes with a *p* value <0.1 (169 genes). The HIGH samples showed an upregulation of p53, the negative regulator of the cell cycle, regulation of vascular sprouting, and downregulation of pathways involved in thermogenesis and glycerophospholipid metabolism (Fig. 3F and Fig. S8). The thermogenesis genes contained a large subset of mitochondria-encoded genes (Fig. S9). At week-6 post-irradiation, many metabolic pathways were downregulated, and an increase in antigen processing and presentation via MHC-II was observed. The latter may be explained by the numerous immune cells observed in the irradiated tissue (Fig. 3G and Fig. S10). And finally, at week-20, the HIGH samples displayed downregulation of many metabolic pathways, including pathways involved in mitochondrial organization, transmembrane transport, translation, and the tricarboxylic acid cycle (Fig. S11). In addition, a large cluster of cell adhesion and extracellular structure organization pathways were present that could be linked to the accumulation of extracellular matrix (ECM) in the sinusoids (Fig. 3H and Fig. S12).

Altogether, the transcriptomic analysis shows that day-1 after irradiation, the liver expresses a broad set of genes associated with stress response and repair pathways. At day-6, together with no histological signs of fibrosis, the only detectable 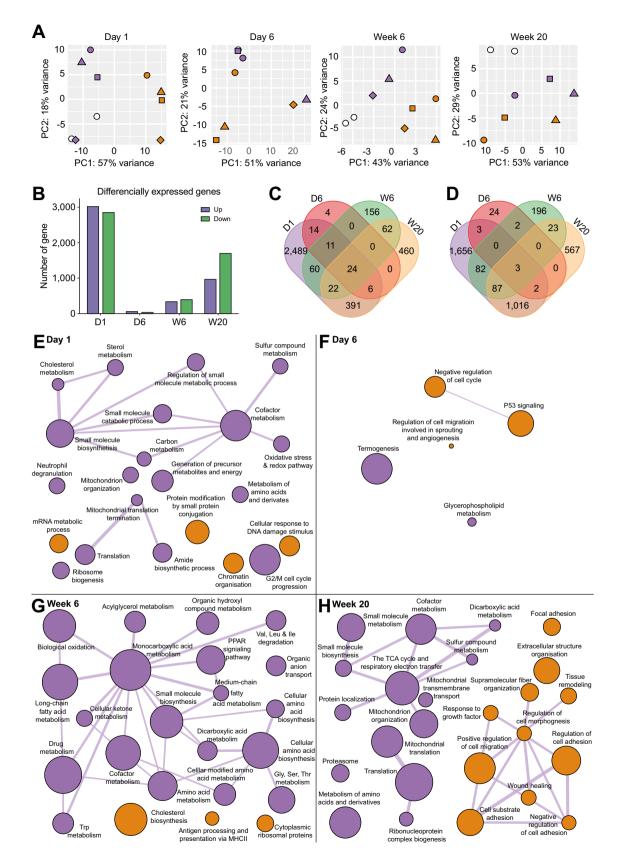regulated pathways included p53, inhibition of cell cycle and thermogenesis. Finally, at week-6 and week-20, when histological signs of fibrosis are present, the number of regulated pathways increased and included tricarboxylic acid cycle genes, immune activation, and extracellular remodeling pathways.

Irradiation induces an increase in mtDNA mutational load and impairs mitochondrial respiratory capacity

Based on our histological and transcriptomic observations, together with the well-documented observation that hepatic fibrosis results from a continued wound healing response to an unresolved injury,[16] we hypothesized that this fibrotic phase may result from the unresolved damage that may be detected on day-6. We looked more closely at the transcriptional activity at day-6, and of the 15 downregulated genes, 6 of them were mitochondria encoding genes. As irradiation was shown to induce extensive damage to mtDNA, resulting in mutations,[17–19] we further assessed the mutational load of mtDNA following irradiation. mtDNA sequences can be investigated using RNAseq data[20]; therefore, we analyzed our RNAseq data from day-1 post-irradiation to evaluate the effect of irradiation on mtDNA integrity. Comparing paired samples collected from HIGH- and LOW-irradiated liver tissue, we found that irradiation significantly increased the heteroplasmic frequency in 10 nucleotide positions. The mutations found were all frameshift mutations in sequences coding for electron transfer chain (ETC) proteins. One mutation affected the ubiquinol cytochrome c reductase (ETC complex III), 2 mutations were located on the cytochrome oxidase (ETC complex IV), and 7 mutations affected genes of the NADH dehydrogenase (ETC complex I) (Fig. 4A). We next evaluated the effect of radiation on the ETC in cultured mouse hepatocytes mimicking the effect we observed at day-6 *in vivo* (Fig. S13A). Hepatocytes were exposed to 0 or 50 Gy gamma radiation, and their viability and ETC function was assessed after 6 days. Irradiation did not decrease hepatocyte viability with stable cell numbers and cell confluency (Fig. 4B,C). To validate the following respirometry experiment, the integrity of mitochondrial membranes was confirmed by the absence of stimulation of respiration by exogenously added cytochrome c (Fig. S13B). The respirometry experiment revealed that irradiation did not modify hepatocytes' basal respiration; however, the maximal respiration was elevated in irradiated cells (Fig. 4D). We hypothesized that the irradiated hepatocytes need to raise their maximal respiration to fulfill a similar basal function due to decreased ETC efficacy. Therefore, we investigated respiratory fluxes over complexes I and IV of the mitochondrial ETC that are partially mitochondrially encoded and complex II, which is entirely nuclear DNA encoded. To enable comparisons between the 2 conditions, we normalized to maximal respiration. Irradiated hepatocytes did not show a modification in complex IV activity. However, they displayed a decreased complex I driven respiration and a compensatory increase in complex II driven respiration, as demonstrated by the absence of difference in complex I+II respiration (Fig. 4E).

Overall, the mouse liver mtDNA sequence analysis revealed an increased heteroplasmy induced by irradiation. Our *in vitro* data suggested an increase in maximal respiratory capacity of the irradiated hepatocytes, allowing them to maintain their basal respiration level. We further showed that complex I driven respiration was decreased and offset by an increase in complex II driven respiration.

Fig. 3. Paired analysis of irradiated and non-irradiated liver transcriptome. Time-dependent PCA analysis displaying the control tissue in black, HIGH-irradiated tissue in red, and LOW-irradiated in blue. The paired HIGH- and LOW-irradiated tissue (coming from the same mouse) were represented with the same shape (A). Bar graph illustrating the numbers of upregulated and downregulated genes issued from comparing the paired HIGH- *vs.* LOW-irradiated sample (B). Venn diagram displaying the upregulated genes (C) and downregulated genes (D) at the different time post-irradiation. Pathway enrichment analysis depicting only the most relevant summary terms for each time point; day-1 $p < 5 \times 10^{-15}$; day-6 $p < 4 \times 10^{-4}$; week-6 $p < 1 \times 10^{-10}$; week-20 $p < 5 \times 10^{-15}$ (Hypergeometric test) (E-H). PCA, principal component analysis.
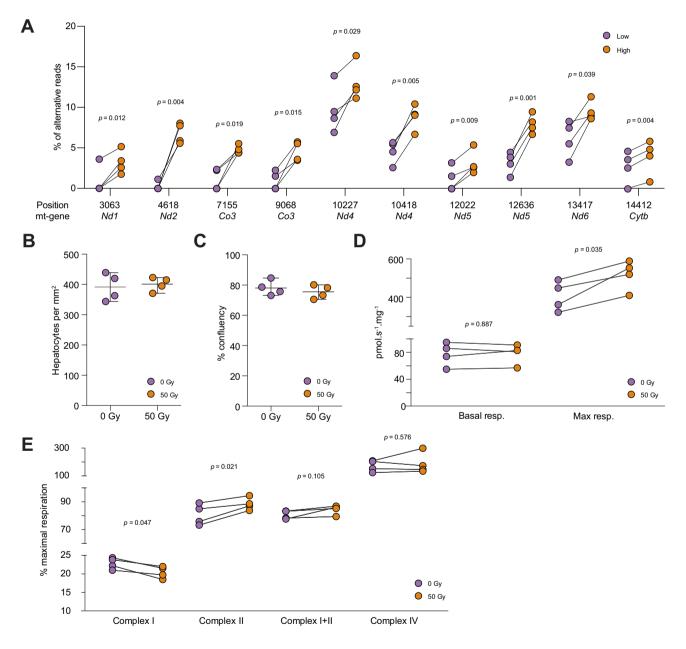
Irradiation led to GSSG/GSH imbalance *in vitro* and *in vivo*
As complex I dysfunction is associated with the production of mitochondrial reactive oxygen species (mtROS),[21] we further checked if increased ROS levels led to a redox imbalance. Firstly, we irradiated cultured hepatocytes with 50 Gy and measured a decrease in reduced glutathione (GSH), and an increase in oxidized glutathione (GSSG) 6 days following irradiation (Fig. 5A). Similarly, the GSH levels *in vivo* were strongly decreased in the highly irradiated liver tissues (HIGH) at day-1 and -6 following irradiation before returning to normal levels at the later time points (Fig. 5B). In parallel, GSSG levels were increased in the high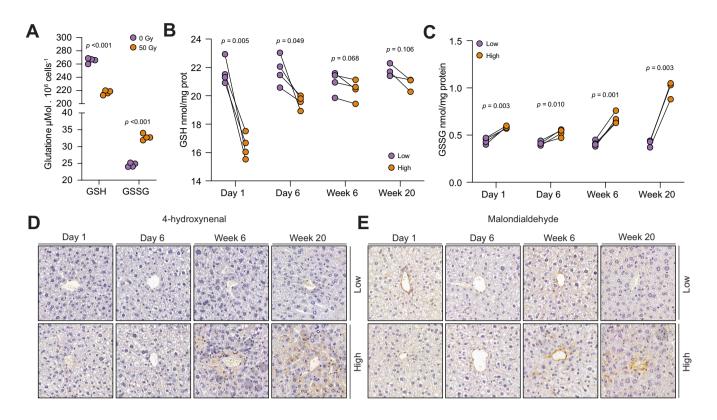ly irradiated liver tissue after day-1 and day-6 and increased to even higher levels during the fibrotic phase at week-6 and week-20 (Fig. 5C).

When antioxidant defense mechanisms are insufficient, ROS reacts with other electron acceptor molecules such as proteins, lipids, nucleic acids, and cellular metabolites.[22] Consequently, the accumulation of lipid peroxides such as 4-hydroxynonenal (4HNE) and malondialdehyde (MDA) can be used to identify the cells with excessive ROS.[23] At day-1 and -6, there were undetectable levels of 4HNE and basal levels of MDA around the central vein and pericentral sinusoidal endothelial cells in both LOW- and HIGH-irradiated liver tissue (Fig. 5D,E). However, at week-6, there was an increase of 4HNE in the cytoplasm of

Fig. 4. **Irradiated mouse hepatocyte displays modified reparation post-irradiation.** Percentage of mtDNA heteroplasmy to the reference mtDNA sequence (AJ512208.1) in the paired LOW- and HIGH-irradiated liver (n = 4) 24 h post-irradiation (paired *t* test) (A). Number (B) and confluency (C) of mouse hepatocyte 6 days after control (n = 4) or irradiation treatment (n = 4). Basal and maximal respiration of hepatocyte cultured following control or irradiation treatment, levels of significance displayed on the graph (paired *t* test) (D), and their basal respiration and complex I, I I+II, and IV activity normalized to the maximal respiration, level of significance displayed on the fig. (paired *t* test) (E). mtDNA, mitochondrial DNA.

Fig. 5. RedOx balance following hepatic irradiation. GSH and GSSG in isolated hepatocytes at day-6 post-irradiation (*t* test) (A). GSH (B), and GSSG (C) in HIGH and its LOW samples at day-1, day-6, week-6, and week-20 following irradiation, levels of significance displayed on the graph (paired *t* test). 4HNE (D) and MDA (E) staining of the HIGH-irradiated liver and its LOW-irradiated counterpart at day-1, day-6, week-6, and week-20 following irradiation. 4HNE, 4-hydroxynonenal; GSSG, oxidized glutathione (glutathione disulfide); GSH, reduced glutathione (glutathione); MDA, malondialdehyde.
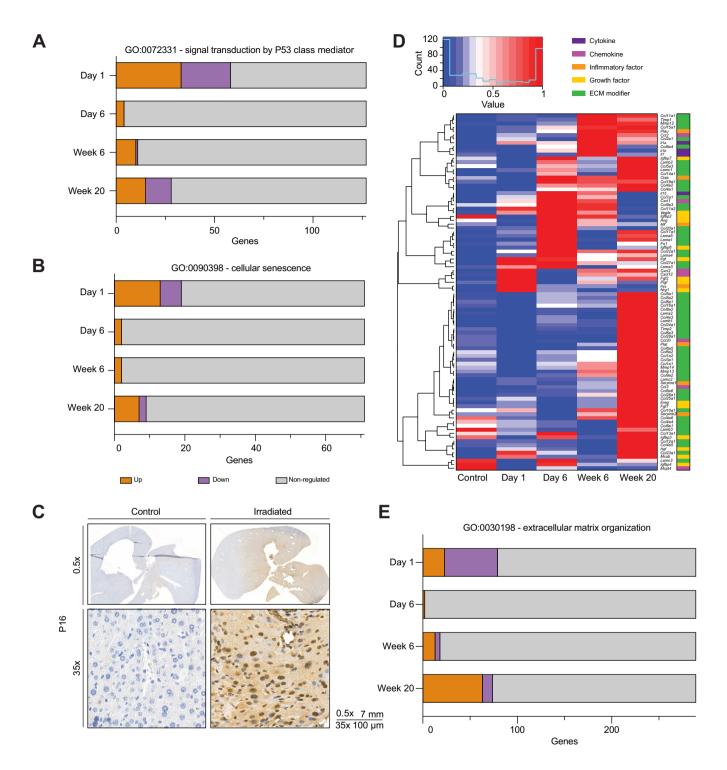
hepatocytes and MDA in endothelial cells, which further increased at week-20 in the HIGH-irradiated tissues (Fig. 5D,E). This late increase in 4HNE and MDA suggests the overloading of the cellular antioxidant defenses in the pericentral cells and correlates with the fibrotic phase of RILD at week-6 and -20.

Irradiation induces an increase of cellular ROS triggering p53, senescence and immune cell infiltration and fibrosis

Increased mitochondrial dysfunction, cellular ROS, and lipid peroxides can affect p53 signaling and senescence.[24,25] Also, senescence in livers of aged mice was associated with pericentral sinusoid collagen deposition.[26] Based on these observations, we questioned if irradiated livers could show a p53 activation leading to a profibrotic senescence-like phenotype. Interestingly, p53 signaling was upregulated in the Metascape pathway analysis at day-6 and week-6 (Fig. S8 and S10). We next looked at genes regulated by the p53 pathway and observed that p53 signaling was strongly regulated at day-1, and after a drop of regulation at day-6, increased again at week-6 and week-20 (Fig. 6A and Fig. S14). Similarly, pathways involved in cellular senescence displayed a congruent profile (Fig. 6B and Fig. S15). Focusing on a pair of p53-regulated senescence-associated genes, *Cdkn1a* (p21[Cip1]) and *Cdkn2a* (p16[INK4a]), we observed that *Cdkn1a* is strongly activated in the irradiated tissue at day-1 and was continuously increased at all time points (Fig. S16A). However, *Cdkn2a* expression was weak in the early time points and increased in HIGH-irradiated tissues by week-20 (Fig. S16B). We further evaluated p16[INK4a] expression in the livers at 20

weeks. At high magnification, we could locate p16[INK4a] in the nucleus of hepatocytes and endothelial cells in the HIGH-irradiated livers (Fig. 6C). At low magnification, p16[INK4a] staining followed the irradiation track, with a maximal staining intensity at the hotspot area associated with the strongest fibrosis (Fig. 6C). Cellular senescence is a stress response that elicits a permanent cell cycle arrest and also triggers profound phenotypic changes such as the production of a bioactive secretome, referred to as the senescence-associated secretory phenotype (SASP), which has been associated with fibrosis.[27] Therefore, we used a list of SASP genes[27] and checked if they were regulated in the HIGH-irradiated samples. First, we observed at weeks-6 and -20 an increase in chemoattractant-related genes, coinciding with the recruitment of immune cells we observed by IMC (Fig 2F). Second, in HIGH-irradiated livers, genes encoding for cytokine genes were increased, coinciding with the activation and proliferation of immune cells as shown by T cells, macrophages, and neutrophil expression of Ki67 and CD44 (Fig. S17). Finally, the ECM-related genes were the most prominent SASP family regulated post-irradiation (Fig. 6D). Thus, we looked at the regulation of the ECM organization pathway and at day-1 post-irradiation, genes involved in ECM organization were mainly downregulated. During the latent phase at day-6, only 2 ECM genes were increased, while at week-6 and week-20, most of the ECM regulating genes were upregulated (Fig. 6E and Fig. S18). Collectively, the HIGH-irradiated liver tissue had an increased expression of p53 senescence-associated genes, including *Cdkn1a* and *Cdkn2a* and SASP factors. Histologically, liver
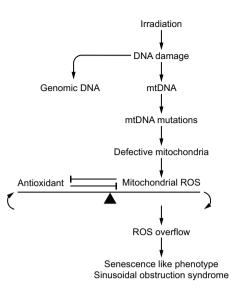
Fig. 6. p53 and senescence promote profibrotic pathways following hepatic radiation. Regulation of genes within the p53 pathway (A), and cellular senescence (B) at the different time points. p16INK4a (*Cdkn2a*) staining 20-weeks post-irradiation at 0.5x and 35x (C). Heat map of regulated SASP (D). Regulation of genes within the extracellular matrix organization (E). ECM, extracellular matrix; SASP, senescence-associated secretory phenotype.

harvested at week-20 post-irradiation displayed an irradiation-specific expression of p16INK4a, consistent with a senescence-like phenotype in the area exhibiting fibrosis.

Altogether, our data support a mechanistic model summarized in Fig. 7, in which irradiation damages mtDNA, which induces mutations and mitochondrial dysfunction (Fig. 4). The

mitochondrial dysfunction leads to the continuous and increasing production of mtROS that leads to cellular antioxidant exhaustion and the interaction of ROS with other biological structures (Fig. 5), resulting in p53 activation (Fig. 6A), a senescence-like phenotype (Fig. 6B and 6C), and immune cell infiltration and activation (Fig 2G, 6D). The combined profibrotic

Fig. 7. From hepatic irradiation to sinusoidal obstruction syndrome. Schematic representation of the proposed mechanism leading to radiation-induced liver disease. mtDNA, mitochondrial DNA; ROS, reactive oxygen species.

effect of mitochondrial dysfunction,[28] lipid peroxide,[29] p53 activation,[30] and immune cell recruitment and activation,[31] results in increased ECM reorganization (Fig. 6E) and the obstruction of the pericentral sinusoid in the HIGH-irradiated tissue (Fig. 2D).

Discussion

Even with IGRT, radiation-induced liver toxicity is still a factor limiting the use of radiotherapy to treat hepatic tumors.[32] Therefore, we sought to establish a mouse model to gain more insight into the mechanisms underlying RILD.

To establish this model, special attention was given when choosing the mouse strain and diet to increase our chance of seeing SOS develop post-irradiation. First, BALB/c mice were used as they are more prone to developing periportal liver fibrosis and more sensitive to total body irradiation than C57BL/6 mice.[12,13] Second, female mice were preferred as previous reports showed an increased fibrosis susceptibility in females.[10] Finally, mice were fed with a standardized diet containing low antioxidants, previously used in a chemotherapy-induced SOS model and described to increase the pericentral fibrosis.[15]

Next, we had to consider the radiosensitivity of the surrounding organs such as the lung, stomach, intestine, kidney, and skin, as all those organs develop severe reactions at doses lower than the liver.[33] The optimal irradiation plan consisted of a 180° arc, with a 5 mm diameter collimator, delivering 50 Gy as a single dose. With this protocol, the surrounding organs and acute radiation toxicity were avoided. Based on clinical data, it is known that the development of RILD requires a sufficient dose of irradiation to be delivered to a large volume of the liver; for example, in humans, irradiating two-thirds of the liver with 50 Gy results in a 5% chance of developing RILD.[6] Therefore, we anticipated that our irradiation plan would not be sufficient to reach irradiation-induced liver insufficiency but could trigger a fibrotic response in the HIGH-irradiated area. In patients, RILD

usually develops after a latency phase of about 4 to 10 weeks following irradiation.[5] Similarly, our model did not show signs of SOS or fibrosis at day-1 and -6, but showed progressive sinusoid obstruction at 6 and 20 weeks post-irradiation. As expected, our treatment did not achieve liver insufficiency within the 20-weeks follow-up. However, based on the extension of the fibrotic area and expression of p16[INK4a] observed at week-20, we cannot completely rule out the possibility of progression to later hepatic insufficiency. However, to ensure the development of full liver failure, experimental protocols in which the of volume irradiated liver tissue is increased and/or the dose delivered is incrementally increased, while sparing surrounding organs, would need to be tested.

As one would anticipate, the transcriptomic analysis highlighted a strong transcriptional response 1-day post-irradiation, capturing the acute response to the injury phase. There were very few differentially expressed genes at day-6 and an increasing number at week-6 and -20. Based on the general understanding of liver biology, the liver will respond to injury by regenerating itself to resolve the initiating damage. However, the wound healing response will persist when the liver cannot fix the initial harm, promoting a profibrotic reaction.[16] Hinging on this general knowledge about liver fibrosis we hypothesized that SOS results from unresolved damage that can be seen 6 days post-irradiation. At this time point, the pathways regulated were associated with p53, thermogenesis, and among the regulated genes, many were encoded by mtDNA. With this in mind, we screened for mechanistic cues in other conditions that induce SOS. Among them, platinum-based chemotherapy,[15] monocrotaline,[34] hematopoietic cell transplantation,[35] and aging,[26] were all associated with mitochondrial dysfunction. Platinum-based chemotherapy was shown to have a 300-fold higher affinity to mtDNA than genomic DNA.[36] The mtDNA-platinum adducts were shown to induce mitochondrial ETC dysfunction and have been proposed to explain the neuropathic side effects.[37] Similarly, irradiation was shown to cause greater DNA damage to mtDNA than genomic DNA.[17] Although the mtDNA repair is not entirely understood, it is described as error-prone,[38] resulting in mtDNA mutations post-irradiation.[39] Our model could point out 12 positions with increased heteroplasmy 24 h post-irradiation in the treated HIGH compared to LOW liver tissue from the same animals.

MtDNA is all coding DNA, and mutations directly affect proteins that take part in the mitochondrial ETC and result in mitochondrial dysfunction.[40] The sequencing data revealed significant increases in frameshift mutations in 7 genes of ETC complex I, 2 genes of ETC complex IV, and 1 gene of ETC complex III. *In vitro*, irradiated hepatocyte mitochondria decreased normalized basal respiration, suggesting a decline in mitochondrial ETC efficacy. Further examination of the complex I, II, and IV activity revealed a reduction in complex I activity compensated by an increase in complex II activity, whereas complex IV activity was not affected. Interestingly, the ETC complex I was shown to release large quantities of mtROS upon dysfunction or inhibition.[21] As we found complex I to be affected by irradiation, we anticipated mitochondrial dysfunction and mtROS production. Similarly, monocrotaline, known to induce SOS, inhibits mitochondrial ETC complex I through its metabolite, dehydromonocrotaline,[41] suggesting the importance of the complex I-dependent mtROS production in SOS development. Finally, mitochondrial dysfunction was shown to lead to the release of mitochondrial content such as mtDNA, mtROS, cardiolipin, and

mitochondrial Ca2+ in the cytoplasm and the extracellular space that can act as proinflammatory molecules.[42]

In the irradiated mouse livers, there was a lower amount of reduced glutathione a day after irradiation and an increase in oxidized glutathione, which was more pronounced at later time points, suggesting an increase in oxidizing agents. When the cellular antioxidant defenses are overwhelmed, ROS freely reacts with other biological structures such as lipids, forming lipid peroxide.[43] In our HIGH-irradiated tissues, 4-HNE and MDA were increased specifically in the pericentral hepatocytes and endothelial cells during the fibrotic phase at week-6 and -20 post-irradiation. This lipid peroxide increase is evidence of a shortage of antioxidants and suggests that both cell types have developed mitochondrial damage. To build our *in vivo* model, we used the low antioxidant diet used to develop the chemotherapy-induced SOS. In their experiment, standard grain-based chow or antioxidant supplementation prevents SOS.[15] Furthermore, using high vitamin E derivatives to increase mitochondrial antioxidant capacity was proven to be radio-protective[44] and reduce mitochondrial dysfunction and peroxide production.[45] Moreover, TXNRD2, a mitochondrial thioreductase enzyme with a role in lowering oxidized mitochondrial proteins, was shown to affect subdermal fibrosis post-irradiation. Patients harboring *Txnrd2* missense mutations showed a modification of their redox balance, resulting in heightened fibrosis after irradiation.[46] Globally, our data and the literature demonstrate the importance of mtROS in the development of radiation-induced normal tissue toxicity.

Our results suggest that irradiation can generate mtDNA mutations, resulting in the activation of p53 and senescence-associated transcripts, especially p21[Cip1] and p16[INK4a]. Further evaluation of p16[INK4a] expression by histology revealed a radiation-dependent expression of p16[INK4a] that colocalizes with the fibrotic tissue. Furthermore, our results indicate an increase in SASP with an increase in chemokines that can explain the presence of neutrophils, macrophages, and T cells and an increase of cytokines that activates the recruited immune cells. In addition, SASP includes ECM factors that are significantly increased at the late time point post-irradiation. These observations fit nicely with the pericentral sinusoidal collagen deposition that was reported in aged livers.[26]

In conclusion, our newly established preclinical RILD model allowed us to study the development of radiation-induced fibrosis in the liver. Our findings on the role of mitochondria in disease development strongly correlate with findings in other etiologies leading to SOS, and other irradiation-induced toxicities.[47–49] Preventing mitochondrial damage in non-malignant liver cells at the time of irradiation may prove a suitable strategy to reduce the risk of RILD and open new therapeutic opportunities for the treatment of liver cancers.

Abbreviations

4HNE, 4-hydroxynonenal; CV, central vein; ECM, extracellular matrix; ETC, electron transfer chain; GSSG, oxidized glutathione (glutathione disulfide); GSH, reduced glutathione (glutathione); HSCs, hepatic stellate cells; IGRT, image-guided radiation therapy; IHC, immunohistochemistry; IMC, imaging mass cytometry; MDA, malondialdehyde; mtDNA, mitochondrial DNA; mtROS, mitochondrial reactive oxygen species; rcf, relative centrifuge force; RILD, radiation-induced liver disease; RNAseq, RNA sequencing; ROS, reactive oxygen species; RT, radiation therapy; SASP, senescence-associated secretory phenotype; SOS, sinusoidal obstruction syndrome; SNP, single nucleotide polymorphism.

Conflict of interest

The authors declare no conflicts of interest that pertain to this work.

Please refer to the accompanying ICMJE disclosure forms for further details.

Authors' contributions

Nicolas Melin: conceptualization, methodology, validation, formal analysis, investigation, data curation, writing the original draft, review & editing, visualization. Tural Yarahmadov: Software, Formal Analysis, Investigation, Data Curation, Visualization, writing review & editing. Daniel Sanchez-Taltavull: Software, Formal Analysis, Investigation, Data Curation, Visualization, writing review & editing. Tess M. Brodie: conceptualization, methodology, investigation, writing review & editing. Fabienne E. Birrer: conceptualization, methodology, investigation, writing review & editing. Benoît Petit: conceptualization, methodology, investigation, writing review & editing. Andrea Felser: conceptualization, methodology, investigation, writing review & editing. Jean-Marc Nuoffer: conceptualization, methodology, resources, writing review & editing. Marie-Catherine Vozenin: conceptualization, methodology, resources, writing review & editing.

Matteo Montani: investigation, resources, writing review & editing. Evelyn Herrmann: writing review & editing, resources, funding acquisition, supervision. Daniel M. Aebersold: writing review & editing, resources, funding acquisition, supervision. Daniel Candinas: writing review & editing, resources, funding acquisition, supervision. Deborah Stroka: conceptualization, validation, writing the original draft, review & editing, visualization, resources, funding acquisition, supervision.

Data availability statement

RNAseq data are available on the GEO database repository (GSE179782; https://www.ncbi.nlm.nih.gov/geo/query/acc.cgi?acc=GSE179782).

Supplementary data

Supplementary data to this article can be found online at https://doi.org/10.1016/j.jhepr.2022.100508.

References

Author names in bold designate shared co-first authorship

[1] Mahadevan A, Blanck O, Lanciano R, Peddada A, Sundararaman S, D'Ambrosio D, et al. Stereotactic Body Radiotherapy (SBRT) for liver metastasis - clinical outcomes from the international multi-institutional

RSSearch(R) Patient Registry. Radiat Oncol 2018;13(1):26. https://doi.org/10.1186/s13014-018-0969-2.

[2] Gerum S, Heinz C, Belka C, Walter F, Paprottka P, De Toni EN, et al. Stereotactic body radiation therapy (SBRT) in patients with hepatocellular carcinoma and oligometastatic liver disease. Radiat Oncol 2018;13(1):100. https://doi.org/10.1186/s13014-018-1048-4.

[3] **Wang Y**, **Deng W**, Li N, Neri S, Sharma A, Jiang W, et al. Combining immunotherapy and radiotherapy for cancer treatment: current challenges and future directions. Front Pharmacol 2018;9:185. https://doi.org/10.3389/fphar.2018.00185.

[4] Guha C, Kavanagh BD. Hepatic radiation toxicity: avoidance and amelioration. Semin Radiat Oncol 2011;21(4):256–263. https://doi.org/10.1016/j.semradonc.2011.05.003.

[5] Reed Jr GB, Cox Jr AJ. The human liver after radiation injury. A form of veno-occlusive disease. Am J Pathol 1966;48(4):597–611.

[6] Pan CC, Kavanagh BD, Dawson LA, Li XA, Das SK, Miften M, et al. Radiation-associated liver injury. Int J Radiat Oncol Biol Phys 2010;76(3 Suppl):S94–S100. https://doi.org/10.1016/j.ijrobp.2009.06.092.

[7] Geraci JP, Jackson KL, Mariano MS, Leitch JM. Hepatic injury after whole-liver irradiation in the rat. Radiat Res 1985;101(3):508–518.

[8] Yannam GR, Han B, Setoyama K, Yamamoto T, Ito R, Brooks JM, et al. A nonhuman primate model of human radiation-induced venocclusive liver disease and hepatocyte injury. Int J Radiat Oncol Biol Phys 2014;88(2):404–411. https://doi.org/10.1016/j.ijrobp.2013.10.037.

[9] Kim J, Wang S, Hyun J, Guy CD, Jung Y. Hedgehog signaling is associated with liver response to fractionated irradiation in mice. Cell Physiol Biochem 2016;40(1-2):263–276. https://doi.org/10.1159/000452543.

[10] Wang S, Lee K, Hyun J, Lee Y, Kim Y, Jung Y. Hedgehog signaling influences gender-specific response of liver to radiation in mice. Hepatol Int 2013;7(4):1065–1074. https://doi.org/10.1007/s12072-013-9461-0.

[11] **Kurland IJ**, **Broin PO**, **Golden A**, Su G, Meng F, Liu L, et al. Integrative metabolic signatures for hepatic radiation injury. PLoS One 2015;10(6):e0124795. https://doi.org/10.1371/journal.pone.0124795.

[12] Zhang SB, Maguire D, Zhang M, Tian Y, Yang S, Zhang A, et al. Mitochondrial DNA and functional investigations into the radiosensitivity of four mouse strains. Int J Cell Biol 2014;2014:850460. https://doi.org/10.1155/2014/850460.

[13] Shi Z, Wakil AE, Rockey DC. Strain-specific differences in mouse hepatic wound healing are mediated by divergent T helper cytokine responses. Proc Natl Acad Sci U S A 1997;94(20):10663–10668.

[14] Schapiro D, Jackson HW, Raghuraman S, Fischer JR, Zanotelli VRT, Schulz D, et al. histoCAT: analysis of cell phenotypes and interactions in multiplex image cytometry data. Nat Methods 2017;14(9):873–876. https://doi.org/10.1038/nmeth.4391.

[15] Robinson SM, Mann J, Vasilaki A, Mathers J, Burt AD, Oakley F, et al. Pathogenesis of FOLFOX induced sinusoidal obstruction syndrome in a murine chemotherapy model. J Hepatol 2013;59(2):318–326. https://doi.org/10.1016/j.jhep.2013.04.014.

[16] Bataller R, Brenner DA. Liver fibrosis. J Clin Invest 2005;115(2):209–218. https://doi.org/10.1172/JCI24282.

[17] Richter C, Park JW, Ames BN. Normal oxidative damage to mitochondrial and nuclear DNA is extensive. Proc Natl Acad Sci U S A 1988;85(17):6465–6467.

[18] **Zhao XT**, **Feng JB**, Li YW, Luo Q, Yang XC, Lu X, et al. Identification of two novel mitochondrial DNA deletions induced by ionizing radiation. Biomed Environ Sci 2012;25(5):533–541. https://doi.org/10.3967/0895-3988.2012.05.006.

[19] Wilding CS, Cadwell K, Tawn EJ, Relton CL, Taylor GA, Chinnery PF, et al. Mitochondrial DNA mutations in individuals occupationally exposed to ionizing radiation. Radiat Res 2006;165(2):202–207. https://doi.org/10.1667/rr3494.1.

[20] Zhang P, Samuels DC, Lehmann B, Stricker T, Pietenpol J, Shyr Y, et al. Mitochondria sequence mapping strategies and practicability of mitochondria variant detection from exome and RNA sequencing data. Brief Bioinform 2016;17(2):224–232. https://doi.org/10.1093/bib/bbv057.

[21] Murphy MP. How mitochondria produce reactive oxygen species. Biochem J 2009;417(1):1–13. https://doi.org/10.1042/BJ20081386.

[22] Schieber M, Chandel NS. ROS function in redox signaling and oxidative stress. Curr Biol 2014;24(10):R453–R462. https://doi.org/10.1016/j.cub.2014.03.034.

[23] Ayala A, Munoz MF, Arguelles S. Lipid peroxidation: production, metabolism, and signaling mechanisms of malondialdehyde and 4-hydroxy-2-nonenal. Oxid Med Cell Longev 2014;2014:360438. https://doi.org/10.1155/2014/360438.

[24] Haas RH. Mitochondrial dysfunction in aging and diseases of aging. Biology (Basel) 2019;8(2). https://doi.org/10.3390/biology8020048.

[25] Shibata T, Iio K, Kawai Y, Shibata N, Kawaguchi M, Toi S, et al. Identification of a lipid peroxidation product as a potential trigger of the p53 pathway. J Biol Chem 2006;281(2):1196–1204. https://doi.org/10.1074/jbc.M509065200.

[26] Gregg SQ, Gutierrez V, Robinson AR, Woodell T, Nakao A, Ross MA, et al. A mouse model of accelerated liver aging caused by a defect in DNA repair. Hepatology 2012;55(2):609–621. https://doi.org/10.1002/hep.24713.

[27] Coppe JP, Desprez PY, Krtolica A, Campisi J. The senescence-associated secretory phenotype: the dark side of tumor suppression. Annu Rev Pathol 2010;5:99–118. https://doi.org/10.1146/annurev-pathol-121808-102144.

[28] Rangarajan S, Bernard K, Thannickal VJ. Mitochondrial dysfunction in pulmonary fibrosis. Ann Am Thorac Soc 2017;14(Supplement_5):S383–S388. https://doi.org/10.1513/AnnalsATS.201705-370AW.

[29] Parola M, Robino G. Oxidative stress-related molecules and liver fibrosis. J Hepatol 2001;35(2):297–306. https://doi.org/10.1016/s0168-8278(01)00142-8.

[30] Krstic J, Galhuber M, Schulz TJ, Schupp M, Prokesch A. p53 as a dichotomous regulator of liver disease: the dose makes the medicine. Int J Mol Sci 2018;19(3). https://doi.org/10.3390/ijms19030921.

[31] Robinson MW, Harmon C, O'Farrelly C. Liver immunology and its role in inflammation and homeostasis. Cell Mol Immunol 2016;13(3):267–276. https://doi.org/10.1038/cmi.2016.3.

[32] Bang A, Dawson LA. Radiotherapy for HCC: ready for prime time? JHEP Rep 2019;1(2):131–137. https://doi.org/10.1016/j.jhepr.2019.05.004.

[33] Bockbrader M, Kim E. Role of intensity-modulated radiation therapy in gastrointestinal cancer. Expert Rev Anticancer Ther 2009;9(5):637–647. https://doi.org/10.1586/era.09.16.

[34] DeLeve LD, Wang X, Kanel GC, Ito Y, Bethea NW, McCuskey MK, et al. Decreased hepatic nitric oxide production contributes to the development of rat sinusoidal obstruction syndrome. Hepatology 2003;38(4):900–908. https://doi.org/10.1053/jhep.2003.50383.

[35] Akil A, Zhang Q, Mumaw CL, Raiker N, Yu J, Velez de Mendizabal N, et al. Biomarkers for diagnosis and prognosis of sinusoidal obstruction syndrome after hematopoietic cell transplantation. Biol Blood Marrow Transpl 2015;21(10):1739–1745. https://doi.org/10.1016/j.bbmt.2015.07.004.

[36] Yang Z, Schumaker LM, Egorin MJ, Zuhowski EG, Guo Z, Cullen KJ. Cisplatin preferentially binds mitochondrial DNA and voltage-dependent anion channel protein in the mitochondrial membrane of head and neck squamous cell carcinoma: possible role in apoptosis. Clin Cancer Res 2006;12(19):5817–5825. https://doi.org/10.1158/1078-0432.CCR-06-1037.

[37] Canta A, Pozzi E, Carozzi VA. Mitochondrial dysfunction in chemotherapy-induced peripheral neuropathy (CIPN). Toxics 2015;3(2):198–223. https://doi.org/10.3390/toxics3020198.

[38] Krasich R, Copeland WC. DNA polymerases in the mitochondria: a critical review of the evidence. Front Biosci (Landmark Ed) 2017;22:692–709.

[39] Wang L, Kuwahara Y, Li L, Baba T, Shin RW, Ohkubo Y, et al. Analysis of Common Deletion (CD) and a novel deletion of mitochondrial DNA induced by ionizing radiation. Int J Radiat Biol 2007;83(7):433–442. https://doi.org/10.1080/09553000701370878.

[40] Lawless C, Greaves L, Reeve AK, Turnbull DM, Vincent AE. The rise and rise of mitochondrial DNA mutations. Open Biol 2020;10(5):200061. https://doi.org/10.1098/rsob.200061.

[41] Mingatto FE, Dorta DJ, dos Santos AB, Carvalho I, da Silva CH, da Silva VB, et al. Dehydromonocrotaline inhibits mitochondrial complex I. A potential mechanism accounting for hepatotoxicity of monocrotaline. Toxicon 2007;50(5):724–730. https://doi.org/10.1016/j.toxicon.2007.06.006.

[42] **Patergnani S**, **Bouhamida E**, Leo S, Pinton P, Rimessi A. Mitochondrial oxidative stress and "mito-inflammation": actors in the diseases. Biomedicines 2021;9(2). https://doi.org/10.3390/biomedicines9020216.

[43] Auten RL, Davis JM. Oxygen toxicity and reactive oxygen species: the devil is in the details. Pediatr Res 2009;66(2):121–127. https://doi.org/10.1203/PDR.0b013e3181a9eafb.

[44] Ferreira PR, Fleck JF, Diehl A, Barletta D, Braga-Filho A, Barletta A, et al. Protective effect of alpha-tocopherol in head and neck cancer radiation-induced mucositis: a double-blind randomized trial. Head Neck 2004;26(4):313–321. https://doi.org/10.1002/hed.10382.

[45] Zhang JG, Nicholls-Grzemski FA, Tirmenstein MA, Fariss MW. Vitamin E succinate protects hepatocytes against the toxic effect of reactive oxygen

species generated at mitochondrial complexes I and III by alkylating agents. Chem Biol Interact 2001;138(3):267–284.

[46] Edvardsen H, Landmark-Hoyvik H, Reinertsen KV, Zhao X, Grenaker-Alnaes GI, Nebdal D, et al. SNP in TXNRD2 associated with radiation-induced fibrosis: a study of genetic variation in reactive oxygen species metabolism and signaling. Int J Radiat Oncol Biol Phys 2013;86(4):791–799. https://doi.org/10.1016/j.ijrobp.2013.02.025.

[47] Livingston K, Schlaak RA, Puckett LL, Bergom C. The role of mitochondrial dysfunction in radiation-induced heart disease: from bench to bedside. Front Cardiovasc Med 2020;7:20. https://doi.org/10.3389/fcvm.2020.00020.

[48] Shimura T, Sasatani M, Kawai H, Kamiya K, Kobayashi J, Komatsu K, et al. A comparison of radiation-induced mitochondrial damage between neural progenitor stem cells and differentiated cells. Cell Cycle 2017;16(6):565–573. https://doi.org/10.1080/15384101.2017.1284716.

[49] Baselet B, Driesen RB, Coninx E, Belmans N, Sieprath T, Lambrichts I, et al. Rosiglitazone protects endothelial cells from irradiation-induced mitochondrial dysfunction. Front Pharmacol 2020;11:268. https://doi.org/10.3389/fphar.2020.00268.

[50] Birrer F.E., Brodie T.M., Stroka D. 20-target Imaging Mass Cytometry panel for mouse liver FFPE tissue. Cytometry A. Submitted for publication.